The Astrophysical Journal, 826:162 (13pp), 2016 August 1 doi:10.3847/0004-637X/826/2/162

THE IMPACT OF SURFACE TEMPERATURE INHOMOGENEITIES ON QUIESCENT NEUTRON STAR RADIUS MEASUREMENTS

K. G. Elshamouty[1], C. O. Heinke[1], S. M. Morsink[1], S. Bogdanov[2], and A. L. Stevens[1,3]
[1] Department of Physics, University of Alberta, CCIS 4-181, Edmonton, AB T6G 2E1, Canada; alshamou@ualberta.ca
[2] Columbia Astrophysics Laboratory, Columbia University, 550 West 120th Street, NY 10027, USA
[3] Anton Pannekoek Institute, University of Amsterdam, Postbus 94249, 1090 GE Amsterdam, The Netherlands
Received 2016 March 15; revised 2016 May 6; accepted 2016 May 18; published 2016 July 28

ABSTRACT

Fitting the thermal X-ray spectra of neutron stars (NSs) in quiescent X-ray binaries can constrain the masses and radii of NSs. The effect of undetected hot spots on the spectrum, and thus on the inferred NS mass and radius, has not yet been explored for appropriate atmospheres and spectra. A hot spot would harden the observed spectrum, so that spectral modeling tends to infer radii that are too small. However, a hot spot may also produce detectable pulsations. We simulated the effects of a hot spot on the pulsed fraction and spectrum of the quiescent NSs X5 and X7 in the globular cluster 47 Tucanae, using appropriate spectra and beaming for hydrogen atmosphere models, incorporating special and general relativistic effects, and sampling a range of system angles. We searched for pulsations in archival *Chandra* HRC-S observations of X5 and X7, placing 90% confidence upper limits on their pulsed fractions below 16%. We use these pulsation limits to constrain the temperature differential of any hot spots, and to then constrain the effects of possible hot spots on the X-ray spectrum and the inferred radius from spectral fitting. We find that hot spots below our pulsation limit could bias the spectroscopically inferred radius downward by up to 28%. For Cen X-4 (which has deeper published pulsation searches), an undetected hot spot could bias its inferred radius downward by up to 10%. Improving constraints on pulsations from quiescent LMXBs may be essential for progress in constraining their radii.

Key words: pulsars: general – stars: neutron – X-rays: binaries – X-rays: stars

1. INTRODUCTION

One of the most intriguing unsolved questions in physics is the equation of state (EOS) of cold, supranuclear-density matter which lies in the cores of neutron stars (NSs). Since each proposed EOS allows a limited range of values for the NS mass M and radius R, accurate measurements of M and R can be used to constrain the NS EOS (see, for reviews, Lattimer & Prakash 2007; Hebeler et al. 2013; Özel 2013; Haensel et al. 2016; Lattimer & Prakash 2016; Steiner et al. 2016).

While it is possible, in some cases, to obtain accurate NS mass measurements (e.g., Demorest et al. 2010; Freire et al. 2011; Antoniadis et al. 2013; Ransom et al. 2014), it is difficult to determine the NS radius. One method for determining the size of an NS is through a modification of the blackbody radius method (van Paradijs 1979): if the distance, flux, and temperature of a perfect blackbody sphere can be measured, then its radius is also known. Since NSs are not perfect blackbodies, this method has been modified to take into account more realistic spectra. General relativistic effects also make these radius measurements degenerate with mass, providing constraints along curved tracks close to lines of constant $R_\infty = R/\sqrt{1 - 2GM/(Rc^2)}$, where M and R are the NS mass and radius.

The two main types of NSs that this method has been applied to are NSs with Type I X-ray bursts and NSs in quiescent low-mass X-ray binaries (qLMXBs). Some NSs that have Type I X-ray bursts also exhibit photospheric radius expansion (PRE) bursts, and these systems have great potential (Sztajno et al. 1987; Damen et al. 1990; Lewin et al. 1993; Özel 2006) to provide EOS constraints. Observations of PRE bursts and fitting to different spectral models has provided some estimations of the NS mass and radius (Özel et al. 2009; Güver et al. 2010a, 2010b; Suleimanov et al. 2011; Poutanen et al. 2014; Nättilä et al. 2015). However, a variety of uncertainties in the chemical composition of the photosphere, the emission anisotropy, color correction factors, and changes in the persistent accretion flux complicate these analyses (Bhattacharyya 2010; Steiner et al. 2010; Galloway & Lampe 2012; Zamfir et al. 2012; Worpel et al. 2013; Özel et al. 2016).

An alternative approach is to fit the emission from low-mass X-ray binaries during quiescence (qLMXBs). During quiescence, the X-rays are (often) dominated by thermal emission from the quiet NS surface, due to heating of the NS core and crust during accretion episodes (Brown et al. 1998). Non-thermal emission is often present, and typically fit by a power-law; this emission may be produced by accretion, synchrotron emission from an active pulsar wind, and/or a shock between this wind and inflowing matter (Campana et al. 1998; Deufel et al. 2001; Cackett et al. 2010; Bogdanov et al. 2011; Chakrabarty et al. 2014). The thermal emission passes through a single-component atmosphere (typically a few cm layer of H, which would have a mass of $\sim 10^{-20}\,M_\odot$ for ~1 cm; Zavlin & Pavlov 2002) , since the elements gravitationally settle within seconds (Alcock & Illarionov 1980; Hameury et al. 1983). Current physical models of hydrogen atmospheres in low magnetic fields (appropriate for old accreting NSs) are very consistent and reliable (Rajagopal & Romani 1996; Zavlin et al. 1996; Heinke et al. 2006; Haakonsen et al. 2012).

Recent work has focused on qLMXBs in globular clusters, where the distance can be known as accurately as 6% (Woodley et al. 2012), thus enabling stringent constraints on the radius (Rutledge et al. 2002). Observations with *Chandra* and its ACIS detector (high spatial and moderate spectral resolution) or *XMM-Newton* with its EPIC detector (moderate spatial resolution, higher sensitivity) have allowed the

identification and spectroscopy of globular cluster qLMXBs. Several dozen qLMXBs are now known in globular clusters, but only a few provide sufficient flux and have sufficiently little interstellar gas absorption to provide useful constraints (e.g., Heinke et al. 2006; Webb & Barret 2007; Guillot et al. 2011; Servillat et al. 2012). The errors on a few of these measurements are beginning to approach 1 km, or ∼10% (see, e.g., Guillot et al. 2013), at which point they become useful for constraining nuclear physics (Lattimer & Prakash 2001). Indeed, a new *Chandra* observation of the qLMXB X7 in 47 Tuc provides radius uncertainties at the 10% level (Bogdanov et al. 2016).

Thus, it has now become crucially important to identify and constrain systematic uncertainties in the qLMXB spectral fitting method. Previous works have checked the effects of variations between hydrogen atmosphere models (Heinke et al. 2006; Haakonsen et al. 2012), distance errors (Heinke et al. 2006; Guillot et al. 2011, 2013; Heinke et al. 2014; Bogdanov et al. 2016), detector systematics (Heinke et al. 2006; Guillot et al. 2011; Heinke et al. 2014), and modeling of the interstellar medium (Heinke et al. 2014; Bogdanov et al. 2016). The largest systematic uncertainty identified so far is the atmospheric composition. If the accreted material contains no hydrogen (as expected from white dwarfs that make up 1/3 of known LMXBs in globular clusters, Bahramian et al. 2014), then a helium (or heavier element) atmosphere will be produced. Such helium atmospheres will have harder spectra than hydrogen atmospheres, so the inferred radii will be larger, typically by about 50% (Servillat et al. 2012; Catuneanu et al. 2013; Heinke et al. 2014; Lattimer & Steiner 2014). This uncertainty can be addressed by identification of the nature of the donor (e.g., by detecting Hα emission, Haggard et al. 2004, or orbital periods, Heinke et al. 2003).

Another serious concern is the possible presence of temperature inhomogeneities—hot spots—on the surface of the NS. The presence of possible hot spots is a well-known concern when modeling the emission from several varieties of NSs (e.g., Greenstein et al. 1983; Zavlin et al. 2000; Pons et al. 2002). The thermal radiation from the surface can be inhomogeneous if the polar caps of the NS are heated, either through irradiation by positrons and electrons for an active radio pulsar (Harding et al. 2002), or via accretion if the magnetic field of the NS is strong enough to channel accreting matter onto the magnetic poles (Gierliński et al. 2002), or channeling of heat from the core to the poles if the internal magnetic field is of the order of 10^{12} G (Greenstein et al. 1983; Potekhin & Yakovlev 2001; Geppert et al. 2004). The result is pulsed emission from the NS surface, which can be detected if the temperature anisotropy, spot size, geometry relative to the observer, and detector sensitivity are favorable. Note that careful measurement of the shape of the pulsed profile can constrain the ratio of mass and radius, or even both independently (e.g., Morsink et al. 2007; Bogdanov 2013; Psaltis et al. 2014; Miller & Miller 2015); in contrast, in our case, undetected temperature inhomogeneities may bias our method.

If the hot spots are not large or hot enough, or the emission geometry is not favorable, the overall pulsed amplitude may be too low to be detected. However, the undetected hot spots will affect the spectrum of the emitted light, typically hardening the spectrum compared to a star with a uniform temperature. If one were to fit the star's spectrum with a single temperature, the presence of undetected hot spots will cause the inferred temperature to be higher and the inferred radius to be smaller than their true values. The fluxes from qLMXBs are generally so low that it is difficult to conduct effective pulsation searches, leaving open the possibility of hot spots. Investigating the effect of undetected hot spots on the inferred NS radius, in the context of the qLMXBs, is the focus of this paper.

Our goal is to answer three questions. First, what pulsed flux fraction will be produced by hot spots of relevant ranges of size and temperature difference? Since this depends on the angle between the hot spot and NS rotational axis and between the rotational axis and the observer, the results will be probability distribution functions. Detailed calculations for this problem have been done for blackbody emission (Psaltis et al. 2000; Lamb et al. 2009), with angular beaming dependence appropriate for the accretion- and nuclear-powered pulsations observed in accreting systems in outburst. However, this calculation has not been performed specifically for hydrogen atmosphere models (which experience greater limb darkening) at temperatures relevant to quiescent NS low-mass X-ray binaries. Second, given constraints on pulsed flux from a given quiescent NS low-mass X-ray binary, what constraints can we then impose on temperature differentials on the NS surface? Third, how much error is incurred in calculations of the NS mass and radius by spectral fitting to a single-temperature NS, particularly for hot spots within the constraints determined above?

Although many of our calculations are general, we will apply them to the specific cases of the relatively bright ($L_X \sim 10^{33}$ erg s^{-1}), quiescent NS low-mass X-ray binaries X5 and X7 in the globular cluster 47 Tuc, due to their suitability for placing constraints on the NS radius. 47 Tuc is at a distance of 4.6 ± 0.2 kpc (Woodley et al. 2012; Hansen et al. 2013) and experiences little Galactic reddening, $E(B-V) = 0.024 \pm 0.004$ (Gratton et al. 2003). X-ray emission was discovered from 47 Tuc by *Einstein* (Hertz & Grindlay 1983) and resolved into nine sources by *ROSAT* (Hasinger et al. 1994; Verbunt & Hasinger 1998). Spectral analysis of the two bright X-ray sources X5 and X7 in initial *Chandra* ACIS data identified them as qLMXBs with dominantly thermal X-ray emission (Grindlay et al. 2001; Heinke et al. 2003). X5 suffers varying obscuration and eclipses as a result of its edge-on 8.7 hr orbit (Heinke et al. 2003), and has a known optical counterpart (Edmonds et al. 2002).

Deeper (300 ks) *Chandra* ACIS observations provided large numbers of counts, enabling tight constraints on X7's radius, $14.5^{+1.6}_{-1.4}$ km for an assumed 1.4 $M_\odot$ mass (Heinke et al. 2006). However, these spectra suffered from significant pileup, the combination of energies from multiple X-ray photons that land in nearby pixels during one exposure (Davis 2001). Although a model was used to correct for this effect, this pileup model contributed unquantified systematic uncertainties to the analysis and thus the reported constraint is no longer generally accepted (e.g., Steiner et al. 2010). A new, 180 ks *Chandra* observation of 47 Tuc in 2014–2015 was taken with *Chandra*'s ACIS detector in a mode minimizing pileup effects, providing a high-quality spectrum of X7 that enables tight constraints on the radius (Bogdanov et al. 2016). Our simulated spectra below are designed specifically to model the effects of hot spots on this new spectrum of X7.

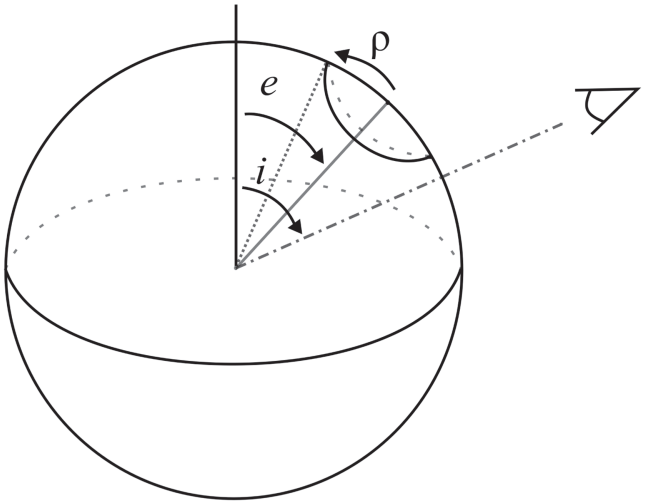

Figure 1. Schematic representation indicating the different angles. The spot's angular radius is ρ, and the emission angle e is the angle between the star's spin axis and the center of the spot. The inclination angle i measures the angle between the spin axis and the direction of the observer.

In addition, extremely deep (800 ks) *Chandra* observations of 47 Tuc have been performed with the HRC-S detector (Cameron et al. 2007), which retains high (microsecond) timing resolution, though it has very poor spectral resolution. This data set enables a search for pulsations from X7 and X5, which we report in this work, utilizing acceleration searches (Ransom et al. 2001). Our constraints on the pulsed fractions from X7 and X5, thus, can enable us to place constraints on the effects of undetected hot spots upon their spectra. Naturally, these constraints are probabilistic in nature, since the orientation of the NS, and of hot spots on it, affects the probability of detecting pulsations from hot spots of a given size and temperature. We also consider what constraints may be obtained from the deeper pulsation limits from *XMM-Newton* observations of the (non-cluster) qLMXB Cen X-4 (D'Angelo et al. 2015).

2. THEORETICAL MODEL

Our model assumes a spherical NS of mass M with radius R and spin frequency f. The emission from most of the star is at one fixed temperature $T_{\rm NS}$, but with one circular spot with a higher temperature $T_{\rm spot}$. The spot's angular radius is ρ, and the emission angle e is the angle between the star's spin axis and the center of the spot. The inclination angle i measures the angle between the spin axis and the direction of the observer. Figure 1 shows a schematic representation of the angles used in our model. The distance to the star is d and the gas column density is N_H. This leads to a total of 10 parameters to describe the flux from a star with a hot spot.

For most of our calculations, we choose the spot size to match that predicted by the polar cap model (Lyne et al. 2006, Equation (18.4)):

$$\rho = (2\pi fR/c)^{1/2}, \quad (1)$$

where c is the speed of light. This formulation reduces the number of parameters in our problem by one. This appears to be a reasonably adequate approximation for the trend of the size of X-ray emitting hot spots on radio pulsars, as suggested by phase-resolved X-ray spectral fitting of PSR J0437-4715 (Bogdanov 2013), the Vela pulsar (Manzali et al. 2007), PSR B1055-52, and PSR B0656+14 (De Luca et al. 2005). It is not known if this is a good approximation for the spot size for qLMXBs. We will show that the dependence of pulsed fraction on spin frequency (for fixed spot size) is small.

The hydrogen atmosphere model (McClintock et al. 2004; Heinke et al. 2006; similar to that of Zavlin et al. 1996 and Lloyd 2003) assumes a thin static layer of pure hydrogen ($R_{\rm H\text{-}atm} \ll R_{\rm NS}$), which allows the use of a plane-parallel approximation. We assume (following, e.g., Bhattacharya & van den Heuvel 1991) that the NS is weakly magnetized ($B \ll 10^9$ G), therefore the effects of the magnetic field on the opacity and EOS of the atmosphere can be neglected. The opacity within the atmosphere is due to a combination of thermal free–free absorption and Thomson scattering. Light-element NS atmosphere models shift the peak of the emission to higher energies, relative to a blackbody model at the same effective surface temperature, due to the strong frequency dependence of free–free absorption (Romani 1987; Rajagopal & Romani 1996; Zavlin et al. 1996). The opacity of the atmosphere introduces an angular dependence to the radiation which is beamed towards the normal to the surface, leading to a limb-darkening effect (Zavlin et al. 1996; Bogdanov et al. 2007). Limb darkening leads to a higher pulsed fraction compared to isotropic surface emission, since the effects of light-bending and Doppler boosting are reduced (Pavlov et al. 1994; Bogdanov et al. 2007). The flux from the hydrogen atmosphere decreases slightly as the acceleration due to gravity increases, while it increases as the effective temperature increases.

The flux from the star is computed using the Schwarzschild plus Doppler approximation (Miller & Lamb 1998; Poutanen & Gierliński 2003) where the gravitational light-bending is computed using the Schwarzschild metric (Pechenick et al. 1983) and then Doppler effects are added as though the star were a rotating object with no gravitational field. This approximation captures the most important features of the pulsed emission for rapid rotation (Cadeau et al. 2007), except for effects due to the oblateness of the star (Morsink et al. 2007). The oblate shape of the star is not included in the computations done in this paper, since the oblate shape only adds small corrections to the pulsed fraction compared to factors such as the temperature differential and spot size. In addition, it has been shown (Bauböck et al. 2015a) that the oblate shape affects the inferred radius (at the level of a few percent) for uniformly emitting blackbody stars. However, the inclusion of geometric shape effects on the inferred radius for hydrogen atmospheres is beyond the scope of this work. We note that these effects should be even less in hydrogen atmosphere models than in blackbody models, since the limb darkening in the hydrogen atmosphere case reduces the importance of the exact shape of the star.

In order to speed up the computations, we divide the flux calculation into three sections: $F_{\rm spot}$, the flux from only the spot with effective temperature $T_{\rm spot}$ (the rest of the star does not emit); $F_{\rm NS}$, the flux from the entire star with uniform temperature $T_{\rm NS}$; and $F_{\rm backspot}$, which only includes flux from the spot with effective temperature $T_{\rm NS}$. The total observed flux is then

$$F_{\rm obs} = F_{\rm NS} + F_{\rm spot} - F_{\rm backspot}, \quad (2)$$

which depends on photon energy and rotational phase.

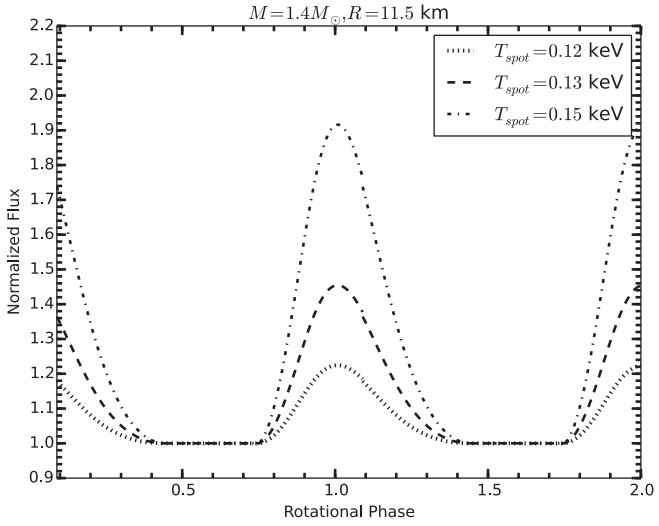

Figure 2. Pulsed profiles for a 1.4 $M_{\odot}$, 11.5 km NS with a hot spot at $i = 86°$ and $e = 85°$ at different temperature differentials. The spin frequency is 500 Hz and $\rho = 20°$.

The computation of $F_{\rm spot}$ is done by first choosing values for M, R, f, ρ, i, e, $T_{\rm spot}$, d, and N_H. The Schwarzschild plus Doppler approximation is used to compute the flux at a distance d from the star assuming that the parts of star outside of the spot do not emit any light.

For the light curve calculation, we first calculate the X-ray absorption by the interstellar medium (using the `tbabs` model with `wilm` abundances, Wilms et al. 2000) on the model array, assuming $N_H = 1.3 \times 10^{20}\,{\rm cm}^{-2}$. The N_H is inferred from the measured $E(B-V)$ using the Predehl et al. (1991) relation. We then fold the flux model array over the *Chandra* HRC effective area and a diagonal response matrix. Finally, the flux is summed over the energy range of the detector (0–10 keV) for each value of rotational phase. The result is the light curve emergent from a hot spot with temperature $T_{\rm spot}$ on the surface of a rotating NS, as detected by *Chandra* HRC. Similarly, $F_{\rm backspot}$ is computed in the same way, except that the effective temperature of the spot is $T_{\rm NS}$ instead of $T_{\rm spot}$. To calculate the emission $F_{\rm NS}$ from the entire uniformly emitting surface, we calculate the predicted flux from the `NSATMOS` model at $T_{\rm NS}$, folded through the `tbabs` model, using the same choices of N_H, M/R, and d. The pulsed fraction, PF, for the *Chandra* HRC is calculated by finding the maximum and minimum values for the observed flux, and computing

$$\mathrm{PF} = (F_{\rm obs,max} - F_{\rm obs,min})/(F_{\rm obs,max} + F_{\rm obs,min}). \quad (3)$$

To compute the expected spectrum, we follow the same procedure for calculating the observed flux ($F_{\rm obs}$), and then integrate the flux over all phase bins at each observed energy. We then incorporate X-ray absorption by the interstellar medium, and fold the flux through the relevant *Chandra* ACIS-S effective area and Response Matrix File (CALDB 4.6.3, appropriate for observations taken in 2010), ending with the phase-averaged absorbed spectrum.

In this paper, we make reference to a fiducial star with the values of $M = 1.4\,M_{\odot}$, $R = 11.5$ km, and $d = 4.6$ kpc. We use a value for the NS effective surface temperature $T_{\rm NS} = 0.100$ keV (or equivalently $\log T_{\rm NS} = 6.06$), which is appropriate for the qLMXBs X5 and X7 in 47 Tuc (Heinke et al. 2003, 2006; Bogdanov et al. 2016).

In Figure 2, we show the normalized pulsed profiles for the fiducial star with different surface temperature differentials. The star spins with frequency 500 Hz, which corresponds to a spot angular radius of 20° in Equation (1). The spot's center is at colatitude 85° and the observer's inclination angle is 86°. Naturally, there is a strong dependence of the pulsed fraction on the temperature of the spot. The pulsed fraction increases from 16% to 27% when the temperature differential increases by 0.02 keV, from $T_{\rm spot} = 0.13$ keV to $T_{\rm spot} = 0.15$ keV.

3. LIMITS ON THE PULSED FRACTION

We now address the limits on the surface temperature differentials that can be made from observational upper limits on an NS's pulsed fraction. To investigate this, we choose different parameters M, R, f, ρ, and $T_{\rm spot}$ describing the NS and its spot (with $T_{\rm NS} = 0.1$ keV, $N_H = 1.3 \times 10^{20}\,{\rm cm}^{-2}$ fixed for all models). For each choice of these parameters we then simulate the pulsed profiles using the methods described in Section 2 for 300 choices of inclination, i, and emission, e, angles. We select i and e from distribution uniform in $\cos i$, appropriate for random orientations on the sky, and for most of our analyses, a distribution uniform in $\cos e$, random positions of the magnetic axis on the NS. Distributions of an angle that are uniform in the cosine of the angle tend to favor inclinations close to 90°, which produce relatively large pulsed fractions. We note that our assumption of a distribution of e, uniform in $\cos e$, may not be correct, if accreting NSs tend to shift their magnetic poles close to their rotational poles, as suggested in some theories (Chen & Ruderman 1993; Chen et al. 1998; Lamb et al. 2009). Radio polarization studies do not find clear results for millisecond pulsars (Manchester & Han 2004), but there is evidence from gamma-ray light curve fitting (e.g., Johnson et al. 2014) and phase-resolved X-ray spectroscopy (e.g., Bogdanov 2013) that radio millisecond pulsars (descendants of LMXBs) generally have relatively large angles between their magnetic and rotational poles. To explore the effects of differing assumptions about the distribution of e, in our last analysis (on effects of spots on the inferred NS radius) we consider both a distribution uniform in $\cos e$, and one that is uniform in e.

We computed pulsed fractions, using the same model used to generate Figure 2, with values of $T_{\rm spot}$ ranging from 0.105 to 0.160 keV, and a distribution of 300 choices of i and e for each spot temperature. In Figure 3 we plot histograms of the pulsed fractions for each value of the spot temperature.

The peak for each distribution corresponds to choices of i and e being close to 90°, which give the highest pulsed fraction, while the tail of the i and e distributions extend to 3° with very small probability. As expected, as the temperature differential between the spot and the rest of the star increases, the typical pulsed fraction increases, while a tail of low pulsed fraction simulations is always present. Similarly, the spot size correlates strongly with pulsed fraction. In Figure 4, we vary spot size while keeping all other parameters constant. Here, Equation (1) was not used to relate spin frequency and polar cap size, instead keeping the frequency fixed. In Table 1, we show the 90th percentile upper & lower limits on pulsed fraction for a wide range of angular spot sizes ρ and spot temperatures.

We now explore the importance of the polar cap model, Equation (1), linking the angular spot size to the spin frequency. First, consider the effect of choosing the spin

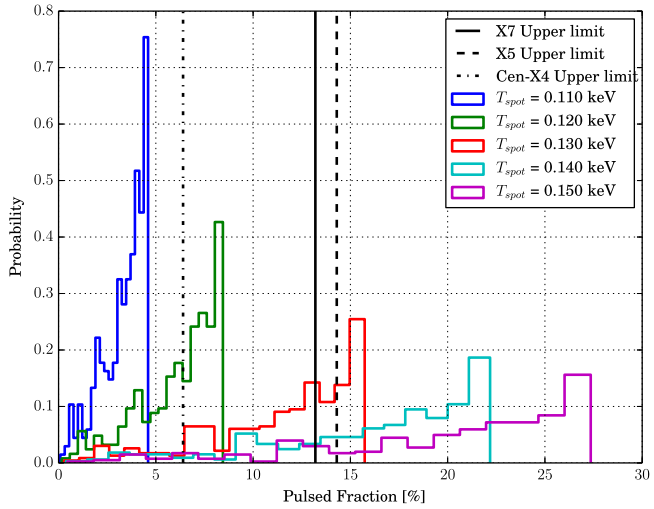

Figure 3. Histograms of simulated pulsed fractions for the fiducial NS with 300 different combinations of i and e for five different temperature differentials. The spin frequency is fixed at 500 Hz and the spot angular radius is $\rho = 20°$. The NS surface's effective temperature is fixed at 0.10 keV with $M = 1.4\,M_{\odot}$ and $R = 11.5$ km.

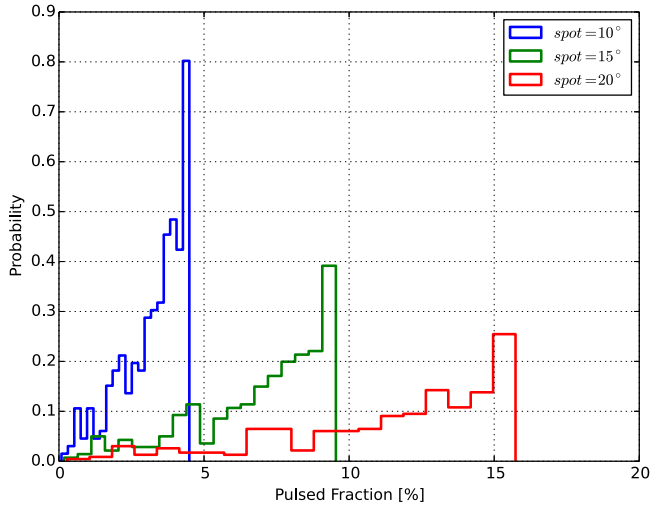

Figure 4. Effect of angular spot radius on the histogram of pulsed fractions for 300 values of i and e. For each histogram the NS parameters were fixed at $M = 1.4\,M_{\odot}$, $R = 11.5$ km, $T_{\rm NS} = 0.10$ keV, $T_{\rm spot} = 0.13$ keV, and $f = 500$ Hz.

frequency independent of the spot size. As the star's spin increases, the Doppler boosting increases, which increases the intensity of the blueshifted side of the star, which will increase the pulsed fraction. This effect is shown in Figure 5, where it can be seen that increasing the star's spin frequency does increase the pulsed fraction. However, the effect is quite small, since the pulsed fraction increases only by 2% when the frequency increases from 100 to 500 Hz. This should be contrasted with Figure 4 where the effect of changing the spot size but keeping the spin frequency fixed is shown. Increasing the angular spot radius by a factor of two increases the maximum pulsed fraction by a factor of three.

The choice of mass and radius affects the pulsed profile through two physical effects. First, the ratio of M/R controls the angles through which the light rays are bent. Larger M/R gives a more compact star, which produces more gravitational bending. This leads to more of the star being visible at any time, which produces a lower pulsed fraction (Pechenick et al. 1983), as can be seen in Figure 6. Second, increasing the surface gravity (where $g = GMR^{-2}/\sqrt{1 - 2GM/Rc^2}$) alters the emission pattern, decreasing the limb darkening, which decreases the pulsed fraction. The effect of the surface gravity is shown in Figure 7 where different values of M and R are chosen so that the ratio M/R is kept constant. The largest star

Table 1
Upper and Lower Limits on Pulsed Fractions for a 1.4 $M_{\odot}$, 11.5 km NS at Effective Surface Temperature 0.100 keV ($\log T = 6.06$)

$T_{\rm spot}$ (keV)	ρ (°)	f (Hz)	PF	
			90%<	90%>
0.105	20	500	2.3	0.9
0.110	20	500	4.4	1.8
0.115	20	500	6.4	2.5
0.120	20	500	8.2	3.3
0.125	20	500	11.6	4.8
0.130	20	500	15.4	6.6
0.135	20	500	18.7	7.9
0.140	20	500	21.7	9.2
0.145	20	500	24.4	10.3
0.150	20	500	26.8	11.3
0.155	20	500	30.1	12.6
0.160	20	500	34.8	14.5
0.105	24	716	3.7	1.4
0.110	24	716	7.0	2.6
0.115	24	716	9.9	3.8
0.120	24	716	12.6	4.9
0.125	24	716	17.3	6.8
0.130	24	716	22.5	9.0
0.135	24	716	26.9	11.0
0.140	24	716	30.7	12.7
0.145	24	716	33.9	14.1
0.150	24	716	37.3	15.5
0.155	24	716	41.1	17.1
0.160	24	716	46.3	19.3

Note. Results for Monte Carlo simulations of 300 choices of i and e (drawn from distributions uniform in $\cos i$ and $\cos e$) for each choice of spot temperature and rotation rate. The spot size is determined by the polar cap model. The two right-hand columns represents the upper and lower 90% bounds on the pulsed fraction.

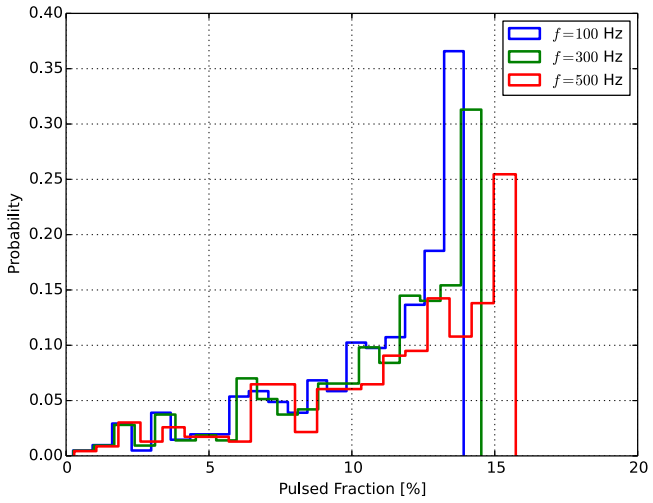

Figure 5. Effect of spin frequency on the histogram of pulsed fractions for 300 values of i and e. For each histogram the NS parameters were fixed at $M = 1.4\,M_{\odot}$, $R = 11.5$ km, $T_{\rm NS} = 0.10$ keV, $T_{\rm spot} = 0.13$ keV, $\rho = 20°$.

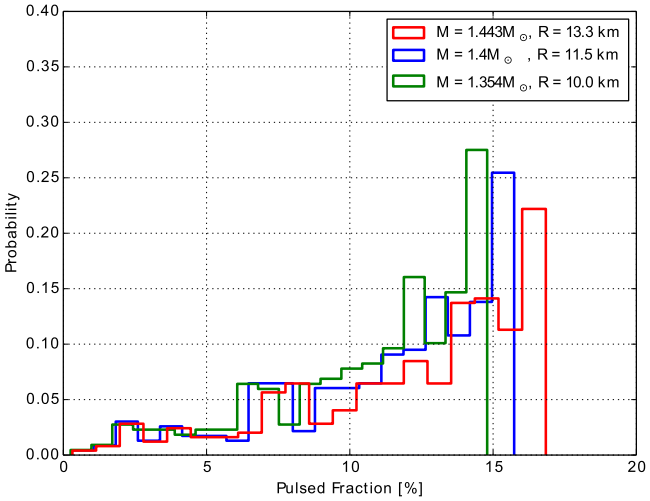

Figure 6. Effect of M/R on the histogram of pulsed fractions for 300 values of i and e. The choices of M/R values are 0.16, 0.18, and 0.2 for the red, blue, and green histograms, respectively. For each histogram the NS parameters were fixed at $T_{\rm NS} = 0.10$ keV, $T_{\rm spot} = 0.13$ keV, $f = 500$ Hz, and $\rho = 20°$. Values of mass and radius are chosen so that $\log g = 14.244$.

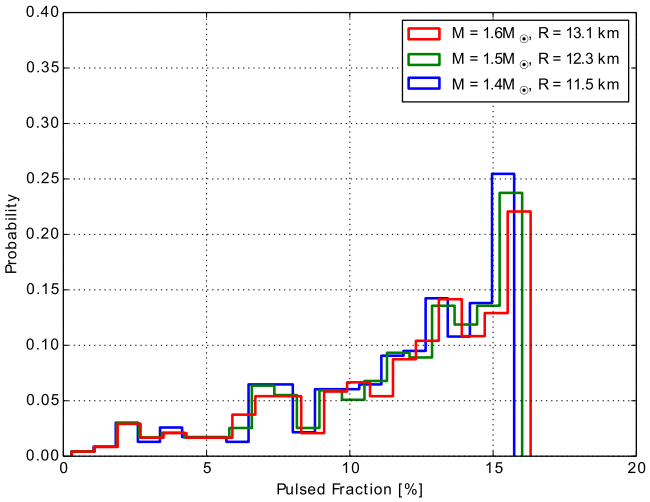

Figure 7. Effect of surface gravity on the histogram of pulsed fractions for 300 values of i and e. The choices of $\log g$ are 14.186, 14.214, and 14.244 for the red, blue, and green histograms. For each histogram the NS parameters were fixed at $M/R = 0.18$, $T_{\rm NS} = 0.10$ keV, $T_{\rm spot} = 0.13$ keV, $f = 500$ Hz, and $\rho = 20°$.

has the lowest surface gravity and the largest pulsed fraction. Both effects are small, with changes in M/R causing changes in the pulsed fraction of a similar order as the changes due to spin frequency. The effects due to surface gravity changes are even smaller. All of these effects act to increase the pulsed fraction if the radius of the star is increased while keeping the mass constant, as shown by Bogdanov et al. (2007).

In this work, we simulate the effects of one spot. Adding a second spot would typically reduce the measured pulsed fraction. This depends on the compactness of the star, on the angles e and i, and on whether the spots are antipodal. For angles e and i near 90°, one spot will always be visible (for typical NS compactness values, such as our 11.5 km, 1.4 $M_\odot$ standard star), which will reduce the pulsed fraction. However, if the angles e and i are both far from 90°, then the far spot will not be strongly visible and the pulsed fraction will not change dramatically. Thus, the effect on the histograms of pulsed fractions will be to shift the peak to smaller values, but the tail at low values (which is made up of realizations with small values of e and/or i) will be much less affected. The 90th percentile lower limits on the pulsed fraction are set by the tail at low values, so the pulsed fraction lower limits will generally not be strongly affected by adding a second spot (assuming it is antipodal to the first spot).

Table 2
Chandra HRC Archival Data of Globular Cluster qLMXBs

Cluster/source	ObsID	Date	Exposure (ks)
47 Tucanae	5542	2005 Dec 19	50.16
X5 & X7	5543	2005 Dec 20	51.39
	5544	2005 Dec 21	50.14
	5545	2005 Dec 23	51.87
	5546	2005 Dec 27	50.15
	6230	2005 Dec 28	49.40
	6231	2005 Dec 29	47.15
	6232	2005 Dec 31	44.36
	6233	2006 Jan 2	97.93
	6235	2006 Jan 4	50.13
	6236	2006 Jan 5	51.92
	6237	2005 Dec 24	50.17
	6238	2005 Dec 25	48.40
	6239	2006 Jan 6	50.16
	6240	2006 Jan 8	49.29
M28	2797	2002 Nov 8	49.37
Source 26	6769	2006 May 27	41.07

3.1. Application to qLMXBs in 47 Tuc, M28, and Cen X-4

Among globular cluster qLMXBs with thermal spectra, only three (X5 and X7 in 47 Tuc, and source 26 in M28) have substantial observations with a telescope and instrument with the timing and spatial resolution (*Chandra*'s HRC-S camera in timing mode) to conduct significant searches for pulsations at spin periods of milliseconds.[4] These targets have not previously been searched for pulsations.

We extracted light curves from X7 and X5 from 800 ks of *Chandra* HRC-S data, obtained during 2005 December–2006 January, described in Cameron et al. (2007). To search for pulsations from qLXMBs we make use of *Chandra* HRC-S observations, which offer a time resolution of ∼16 μs in the special SI mode. We extracted source events for the 47 Tuc qLMXBs X7 and X5 from mutiple HRC-S exposures acquired in 2005 and 2006 (see Cameron et al. 2007) and the M28 qLMXB (named Source 26 by Becker et al. 2003) from two exposures obtained in 2002 and 2006 (Rutledge et al. 2004; Bogdanov et al. 2011). Table 2 summarizes the archival observations that were used in this analysis. For each source the events were extracted from circular regions of radius 2.″5 centered on the positions obtained from `wavdetect`. The recorded arrival times were then translated to the solar system barycenter using the `axbary` tool in CIAO assuming the DE405 solar system ephemeris. The HRC provides no reliable spectral information so all collected events were used for the analysis below.

[4] Note that Papitto et al. (2013) searched for pulsations from the accreting millisecond X-ray pulsar IGR J18245-2452 during an intermediate-luminosity (1.4×10^{33} erg s^{-1}) outburst, using a 53 ks HRC-S observation of M28 and a known ephemeris for the pulsar, and placed an upper limit of 17% on the pulsed amplitude.

The pulsation searches were conducted using the PRESTO pulsar search software package. Given that NS qLMXBs are by definition in compact binaries, the detection of X-ray pulsations from these objects in blind periodicity searches is complicated by the binary motion of the NS, which smears out the pulsed signal over numerous Fourier bins and thus diminishes its detectability. Therefore, it is necessary to employ Fourier-domain periodicity search techniques that compensate for the binary motion when searching for spin-induced flux variations. For this analysis, we use two complementary methods: acceleration searches and "sideband" (or phase-modulation) modulation searches. For the acceleration search technique, the algorithm attempts to recover the loss of power caused by the large period derivative induced by the rapid orbital motion (Ransom 2002). This method is most effective when the exposure time of the observation is a small fraction of the orbital period. In contrast, the sideband technique is most effective when the observation is much longer than the orbital period, provided that the observation is contiguous (Ransom et al. 2003). This approach identifies sidebands produced in the power spectrum centered around the intrinsic spin period and stacks them in order to recover some sensitivity to the pulsed signal.

The orbital periods of LMXBs are typically of the order of hours, or for the case of ultracompact systems, $\lesssim$1 hr. Due to the relatively low count rates of the three qLMXB sources, searching for pulsations over short segments of the binary orbit ($\lesssim$30 minutes) is not feasible so acceleration searches are insensitive to pulsations from these targets. As the *Chandra* exposures are longer than the orbital cycle of X5 and likely for X7 and M28 source 26 as well, the phase-modulation method is the most effective for this purpose.

The maximum frequency that we search up to sets our number of trials, and thus sets how strong an upper limit we can set. The pulsed fraction limit increases as we go to higher frequencies because it is necessary to bin the event data for the acceleration and sideband searches. This causes frequency dependent attenuation of the signal, resulting in decreased sensitivity at high frequencies (e.g., Middleditch 1976; Leahy et al. 1983). The pulsed fraction upper limits were obtained in PRESTO, which considers the maximum power found in the power spectrum as described in Vaughan et al. (1994). We find no evidence for coherent X-ray pulsations in any of the individual observations of the three qLMXBs. The most restrictive upper limits on the X-ray pulsed fraction were obtained from the longest exposures. We find that for spin periods as low as 2 ms (500 Hz), the 90% upper limit on any pulsed signal 14%, 13%, and 37%, for X5, X7, and M28 source 26.

Performing searches up to the fastest known NS spin period (Hessels et al. 2006), 1.4 ms (716 Hz), the limits are 16%, 15%, and 37%. Since the pulsed fraction upper limit for Source 26 in M28 is so high it does not lead to useful constraints, so we do not consider it further in our analysis.

Our pulsed fraction upper limit on X7 (as an example) places limits on the temperature differentials that the NS may have. For a spin frequency of 500 Hz, the 90% upper limit of 13% can be compared with the pulsed fraction probabilities for different spot temperatures shown in Table 1. For example, for a spot temperature of 0.125 keV, 90% of computed models have a pulsed fraction smaller than 11.6%. In fact, all computed models at this spot temperature (0.125 keV) have pulsed fractions below the 13% upper limit for X7, and so this temperature differential is consistent with the observations. This means that X7 could have an undetected hot spot. However, increasing the spot temperature to 0.130 keV, the histogram plotted in Figure 3 shows that only 58% of our simulations give a pulsed fraction below the 90% upper limit on X7's pulsed fraction. For higher spot temperatures, it becomes more improbable to have an undetected hot spot; that is, a pulsed fraction below the 90% upper limit on the pulsed fraction for X7. We find that a spot temperature of 0.155 keV, or a temperature differential of 0.055 keV, to be the maximum temperature differential allowable for X7. This calculation assumes that X7 is spinning at 500 Hz. For higher spin frequencies, which give a larger spot radius (as we linked frequency to spot radius), we obtain higher pulsed fractions when other inputs are identical. Therefore, the maximum temperature differential allowable slightly decreases to 0.050 keV (spot temperature of 0.150 keV) above which over 90% of the simulations are above the 90% pulsed fraction upper limit of X7. The 90% upper limit on X5's pulsed fraction is only 1% larger than that for X7, which will increase the maximum temperature differential allowable for X5 by a few percent more than allowed for X7 (~0.005 keV larger). Our computations all assume that the NS has $M = 1.4\,M_{\odot}$ and $R = 11.5$ km, however, our results show that the dependence on mass and radius is weak.

Even more stringent constraints are possible from the accreting NS in Cen X-4, which was observed at a similar luminosity as X7, but at a distance of only 1.2 kpc (Chevalier et al. 1989), with a more sensitive X-ray telescope, *XMM-Newton*. D'Angelo et al. (2015) used a deep (80 ks) *XMM-Newton* observation (Chakrabarty et al. 2014), in which the PN camera was operated in timing mode (with 30 μs time resolution), to search for pulsations. D'Angelo et al. utilized a semicoherent search strategy, in which short segments of data are searched coherently and then combined incoherently (Messenger 2011). This analysis assumed a circular orbit, with orbital period and semimajor axis as measured by Chevalier et al. (1989), but left the orbital phase free. D'Angelo et al. calculated a fractional-amplitude upper limit of 6.4% from Cen X-4 in quiescence. This is significantly lower than the pulsed fraction limits in X5 and X7, so it provides a tighter constraint on the temperature differential, as can be seen in Figure 3. If we assume the NS in Cen X-4 to have the same physical properties as X7, then its maximum spot temperature must be smaller. Our simulations show that even with this small upper limit Cen X-4 can have small temperature differentials (up to 0.01 keV) with all simulations being below the pulsed fraction upper limit. The maximum spot temperature the NS in Cen X-4 may have is 0.130 keV, at which 90% of the simulations have pulsed fractions that are above the 90% upper limit. Similarly, for higher frequencies, at 716 Hz, the maximum allowable spot temperature decreases to only 0.125 keV. Next, we address how these possible hot spots could affect spectroscopic inferences of NS radii, and what limits we can place on these effects from our constraints on the pulsed fraction and temperature differential.

4. EFFECT OF A HOT SPOT ON THE SPECTRUM

The existence of a hot spot causes a change in the observed spectrum. To illustrate the effect, we choose an extreme case, corresponding to our fiducial star rotating at 500 Hz spin

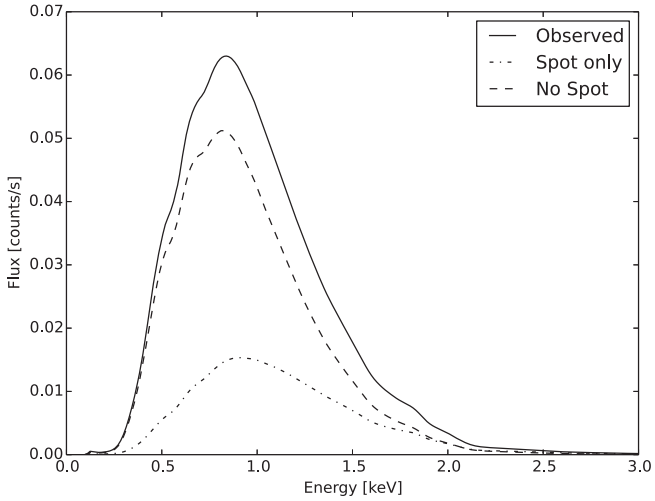

Figure 8. Effect of the existence of hot spots on the observed spectrum. The NS has a surface temperature of 0.10 keV and the hot spot is at 0.15 keV. The peak of the spectrum slightly shifts to a higher energy by 0.02 keV. The hotter the spot is, the more distorted the spectrum will be.

frequency, plus a spot with $T_{\rm spot} = 0.15$ keV, angular radius $\rho = 20°$, and emission and inclination angles $e = 85°$ and $i = 86°$. The pulsed profile for this case is shown in Figure 2 and has a pulsed fraction of 31%. The method described in Section 2 is used to compute the flux from the spot and the rest of the star. We compute the spectra for each rotational phase of the NS over the energy range (0.2–10.0 keV), then we integrate the spectra over all rotational phases to produce the simulated phase-averaged spectrum. We convolve the flux from the spot and star with our interstellar medium model, then fold them over the proper response matrix and effective area of the *Chandra* ACIS-S detector. We fix the exposure time in our simulation at 200 ks (chosen to represent the 2014–2015 *Chandra*/ACIS observation of 47 Tuc), then use a Poisson distribution to select the number of counts per energy bin.

Figure 8 shows an example spectrum. The dashed curve shows the flux $F_{\rm NS}$ integrated over phase, which corresponds to the flux from all parts of a star at $T_{\rm NS} = 0.1$ keV. The dotted curve shows the flux from the hot spot $F_{\rm spot}$, at temperature 0.15 keV. The solid curve shows the observed flux $F_{\rm obs} = F_{\rm NS} + F_{\rm spot} - F_{\rm backspot}$. The peak of the observed spectrum is shifted by ∼0.02 keV and the flux increases by over 20%. The shift of the peak photon energy is smaller than the energy resolution of *Chandra*/ACIS at lower energies (of the order of 0.1 keV).

We now test how the spectroscopically inferred radius changes if the star has a hot spot, but the spectral fitting assumes that the star's emission is homogeneous. We simulated spectra for the fiducial star with $M = 1.4\,M_{\odot}$, $R = 11.5$ km, $T_{\rm NS} = 0.1$ keV, $d = 4.6$ kpc, $f = 500$ Hz, and $N_H = 1.3 \times 10^{20}\,{\rm cm}^{-2}$ with a hot spot on the surface. We chose a variety of temperature differentials and spot sizes (assuming the polar cap model), as shown in Table 3. For each model, we use the heasoft tool `FLX2XSP` to convert the flux array to a PHA spectrum, which we load into `XSPEC` to fit. We let R and $T_{\rm NS}$ be free in the spectral fit, while we fix the mass at $M = 1.4\,M_{\odot}$ and the distance $d = 4.6$ kpc. We allow N_H to be free, but with a minimum value of $1.3 \times 10^{20}\,{\rm cm}^{-2}$. The resulting `XSPEC` fitted values and uncertainties for the radius and temperature are shown along with the reduced chi-squared in Table 3.

Table 3
Best-fit Values for R

$T_{\rm spot}$ (keV)	ρ (°)	f (Hz)	PF (%)	$R_{\rm fit}$ (km)	Log$T_{\rm eff,fit}$	χ^2_ν
...	...	...	...	$11.4^{+0.8}_{-0.7}$	$6.05^{+0.02}_{-0.02}$	0.99
0.13	9	100	3.3	$11.4^{+1.3}_{-0.8}$	$6.04^{+0.02}_{-0.02}$	1.09
0.15	9	100	9.0	$9.7^{+1.1}_{-0.6}$	$6.09^{+0.02}_{-0.02}$	1.09
0.11	20	500	5.5	$11.8^{+1.3}_{-0.8}$	$6.03^{+0.03}_{-0.02}$	1.10
0.12	20	500	9.8	$11.6^{+0.9}_{-0.8}$	$6.04^{+0.02}_{-0.02}$	0.82
0.13	20	500	18.0	$10.9^{+0.8}_{-0.8}$	$6.07^{+0.02}_{-0.02}$	1.15
0.14	20	500	25.2	$9.8^{+0.8}_{-0.6}$	$6.10^{+0.02}_{-0.02}$	1.04
0.15	20	500	30.8	$9.3^{+0.8}_{-0.8}$	$6.11^{+0.02}_{-0.02}$	1.01
0.11	23	667	7.7	$11.6^{+0.8}_{-0.8}$	$6.04^{+0.02}_{-0.02}$	1.06
0.12	23	667	13.9	$10.9^{+0.8}_{-0.6}$	$6.06^{+0.02}_{-0.02}$	0.70
0.13	23	667	24.5	$10.9^{+1.1}_{-0.8}$	$6.07^{+0.02}_{-0.03}$	0.98
0.14	23	667	33.2	$9.1^{+0.9}_{-0.6}$	$6.13^{+0.02}_{-0.02}$	1.18
0.15	23	667	39.5	$8.8^{+1.0}_{-0.4}$	$6.14^{+0.03}_{-0.02}$	1.40

Note. Best-fit values of R and $T_{\rm eff}$ for given choices of $T_{\rm spot}$, spot size ρ, spin frequency, and constant angles $i = 80°$ and $e = 89°$. The spectra are generated assuming $M = 1.4\,M_{\odot}$, $R = 11.5$ km, surface temperature $T_{\rm NS} = 0.10$ keV, and $\log T_{\rm NS} = 6.06$. Errors are 90% confidence. Spectral fits assume $M = 1.4\,M_{\odot}$ and $d = 4.6$ kpc. The pulsed fractions produced by each simulation are provided for reference.

The first row in Table 3 shows the uncertainty inherent in the method by first simulating a light curve for a star with no hot spot; the best-fit radius is quite close (0.1 km) to the input value and the radius uncertainty (0.7–0.8 km) is consistent with that from fitting to real data on X7 (Bogdanov et al. 2016). Next, we see that there is a systematic trend in the inferred radii of the NSs introduced by an undetected hot spot. XSPEC interprets the shifted spectrum as an increase in the temperature of the whole star. However, the observed flux will not be as large as one would expect for the higher temperature, so this is interpreted as indicating a smaller star. The general result is that the star's radius is under-estimated when an undetected hot spot is present. This effect can be seen in many of the best-fit solutions shown in Table 3. The principal factor in introducing bias is the spot temperature; a 15% bias in the average fitted temperature is induced by spot temperatures of 0.14–0.15 keV, for spot sizes between 9° and 23°. For this reason, we focus on the spot temperature as the crucial variable to explore below.

Table 3 only shows results for one particular choice of emission and inclination angles. For a more general picture, for each value of $T_{\rm spot}$ we simulated 300 spectra with emission and inclination angles drawn from distributions uniform in $\cos i$ and $\cos e$ for the fiducial star, assuming a 500 Hz spin, a $1.4\,M_{\odot}$ mass, and a radius of 11.5 km. Each simulation was fit in `XSPEC` using the same method used for Table 3. The resulting 90% confidence limits on the radius from each simulation are indicated by colored dots in Figure 9. Each graph shows the results for a particular spot temperature and has four regions, separated by black lines indicating the input value of the NSs radius R used in the simulation (the "true" radius). The region with $R_{\rm max} \geqslant R$ and $R_{\rm min} \leqslant R$ (lower right-hand quadrant) corresponds to fits that are consistent with the correct radius. The points in the region with $R_{\rm min} > R$ (upper right-hand

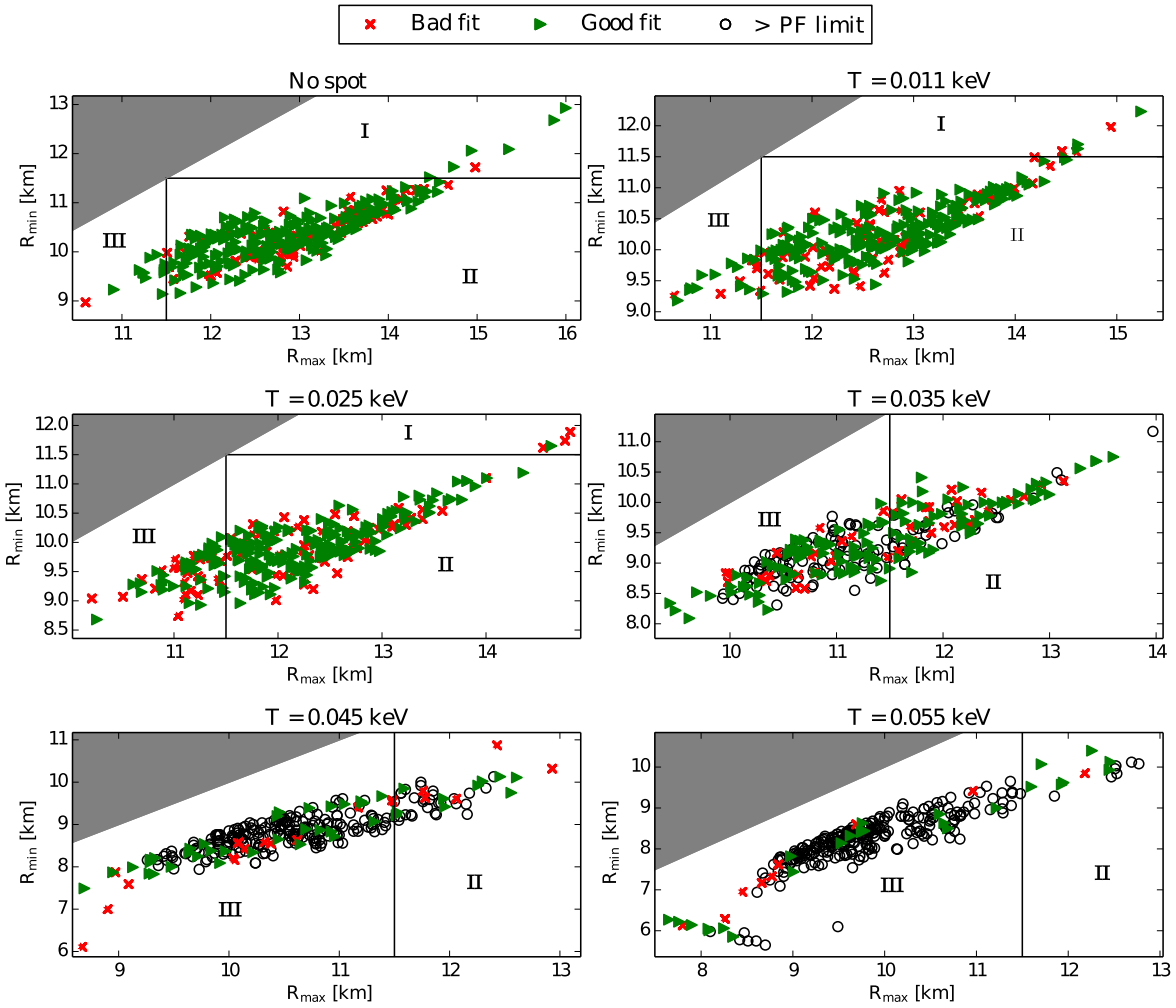

Figure 9. Calculated upper and lower radius limits (90% confidence) from fitting 300 spectral simulations with different choices of the temperature differential, assuming a 1.4 $M_{\odot}$ NS, with the angles e and i chosen from distributions uniform in $\cos i$ and $\cos e$. The shaded area is prohibited and the solid lines represent the "true" (input to simulation) value of the NS radius, $R_{\rm NS} = 11.5$ km. Points in the lower right quadrant of each graph indicate fits where the "true" (input) radius falls between the inferred upper and lower radius limits, while points in the lower left quadrant show a radius upper limit below the "true" value. The results shown here are directly applicable to the NS X7 in 47 Tuc, which has a 90% upper limit of 13% on the pulsed fraction.

quadrant) are fits that overestimate the NSs radius, while the points in the region with $R_{\rm max} < R$ (lower left-hand quadrant) underestimate the radius. The fourth region, shaded gray, is forbidden since it corresponds to $R_{\rm min} > R_{\rm max}$.

To determine whether the spectral distortion due to a hot spot would be detectable, and thus whether NSs with hot spots might be identified by their poor fits to single-temperature models, we retained fit quality information for each fit. We define each fit with a reduced chi-squared value greater than 1.1 (which indicates a null hypothesis probability less than 0.044, given the 51 degrees of freedom) to be a "bad" fit, and mark it as a red cross. Unfortunately, the fraction of "bad" fits does not increase substantially with increasing hot spot temperature (Figure 9, and Table 4), indicating that fit quality cannot effectively identify spectra with hot spots.

Each simulation also has an associated pulsed fraction. If the pulsed fraction is larger than the measured upper limit for X7 (for an assumed spin of 500 Hz), we marked it as a black hollow circle. Good fits that do not violate the pulsed-fraction limit are marked as a green triangle. For spot temperatures up to 0.125 keV we find that over 75% of the simulations give inferred radii that are consistent with the true value of $R_{\rm NS}$. For higher temperature differentials ($T_{\rm spot} > 0.13$ keV) a large fraction of the inferred radii are biased downward from the "true" value by larger than 10% of the true radius of the NS, while the majority (>58%) of the simulations are below the X7 pulsed fraction upper limit. This pulsed fraction limit, and the inferred bias, changes if the spin frequency (and consequently the spot size) changes. For the higher spin frequency of 716 Hz we find that inferred radii can be biased up to 15% smaller than the true radius of the NS for $T_{\rm spot} = 0.13$ keV. In Table 4, we summarize the percentage of inferred radii consistent with the "true" value, the percentage of good fits, and the average bias in the inferred radius for different choices of spot temperature. We examined the behavior of $(R_{\rm max} + R_{\rm min})/2$ versus $R_{\rm fit}$, finding a well-behaved linear relationship between the two quantities. In this paper we calculate the bias as the difference between the median of the inferred $R_{\rm fit,no\ spot}$ radii with no hot spots and the median of the inferred radii $R_{\rm fit,spot}$ with a hot spot, divided by the latter. (This definition allows this bias to be directly applicable to observed radius estimates). The $R_{\rm fit,no\ spot}$ values are results of fitting 300 simulated spectra from a Poisson distribution, which would give a distribution of $R_{\rm fit}$ peaked at the *true* value of $R = 11.5$ km.

Table 4
Bias in Inferred Radii

T_{spot} (keV)	f (Hz)	<X7 limit (%)	<Cen-X4 limit (%)	Consistent (%)	Good fits (%)	Bias (%)
0.105	500	100 (100)	100 (100)	93	79	−0.3
0.110	500	100 (100)	100 (100)	92	75	−0.4
0.115	500	100 (100)	87 (89)	90	78	−1
0.120	500	100 (100)	45 (56)	84	73	−2
0.125	500	100 (100)	22 (34)	76	69	−5
0.130	500	58 (64)	10 (26)	55	73	−10
0.135	500	33 (47)	8 (20)	38	72	−14
0.140	500	24 (38)	7 (16)	19	71	−17
0.145	500	21 (33)	6 (14)	15	69	−20
0.150	500	17 (31)	5 (12)	9	76	−22
0.155	500	12 (28)	3 (10)	5	71	−28
0.160	500	8 (23)	2 (8)	0.6	57	−32
0.105	716	100	100	89	77	−1
0.110	716	100	73	87	79	−2
0.115	716	100	32	86	78	−3
0.120	716	100	21	79	79	−3
0.125	716	63	9	62	79	−8
0.130	716	32	7	33	77	−13
0.135	716	22	6	16	74	−19
0.140	716	17	4	10	72	−23
0.145	716	13	3	5	67	−26
0.150	716	10	3	4	65	−31
0.155	716	8	2	2	56	−38
0.160	716	7	2	0.6	57	−41

Note. For different spot temperatures, the bias (right column) in radius determinations, and the percentages of simulations that lie under the upper limits on the pulsed fraction for X7 and Cen X-4, that give spectral fits consistent with the "true" radius and that give "good" fits ($\chi^2_\nu < 1.1$). Each line gives results from fitting 300 simulated spectra using $R = 11.5$ km and surface temperature $T_{NS} = 0.10$ keV for different choices of spot temperatures and spin frequency. Spectral fits assume $M = 1.4\,M_\odot$ and $d = 4.6$ kpc. The percentage of "good fits" are the percentage of the simulations below the upper limits. Numbers in brackets are for simulations performed with a uniform distribution of e (rather than uniform in $\cos e$).

In Figure 10, we present histograms of the inferred R_{fit} at different spot temperatures, and compare it to the distribution of inferred R_{fit} with no spot. This shows the bias in the mean between the histogram with no spot and the histogram of inferred radii with a hot spot. For a spot temperature as high as 0.125 keV, the bias in R_{fit} is still at or below 5%. At 0.130 keV, the majority of simulations do not violate the pulsed fraction limit, the bias in the mean is 10%, and over half the fits are consistent with the input radius. For the maximum spot temperature we allow in our simulations, the bias in the mean of R_{fit} can reach up to 40%, however <10% of the simulations at this spot temperature are below the upper limits for either X7 or Cen X-4.

To identify a reasonable limiting case, we choose the T_{spot} where less than 10% of the simulations provide pulsed fractions below the upper limit on each NSs pulsed fraction; thus, 0.155 keV for X7 and 0.130 keV for Cen X-4. This allows a maximum downward bias in their spectroscopically inferred radii of up to 28% for X7 and 10% for Cen X-4. For example, if we assume the NS in Cen X-4 to be a $1.4\,M_\odot$ star spinning at 500 Hz with a spectroscopically inferred radius of exactly 11.5 km, an undetected hot spot could allow a true radius as high as 12.65 km. For X7, in the case of maximal undetected hot spots, the measured radius of $11.1^{+0.8}_{-0.7}$ km (for an assumed $1.4\,M_\odot$ NS mass, Bogdanov et al. 2016) could allow a true radius up to 15.2 km in the extreme case. In Figure 11 we summarize the bias in R_{fit} versus spot temperature at 500 and 716 Hz frequencies. At both frequencies, the bias is below 10% for relatively small spot temperatures (up to 0.125 keV). However, at higher spot temperatures (>0.130 keV) there is a clear divergence between the magnitude of the biases at 500 Hz and 716 Hz, becoming larger with spot temperature. Increasing the frequency from 500 to 716 Hz changes the bias from 32% to 41% at the highest spot temperature (0.160 keV), but since the 716 Hz frequency also has a larger pulsed fraction for the same spot temperature, the maximum spot temperature is reduced in the 716 Hz case, and the actual maximum bias in the 500 and 716 Hz cases is similar. Finally, we ran the simulations with choices of a uniform distribution of e and $\cos i$. This produces lower pulsed fractions when compared to simulations using a uniform distribution of $\cos e$ at the same spot temperature (see numbers in parentheses in Table 4). In turn, this increases the maximum allowable spot temperature that would not give rise to detectable pulsations. For X7, the maximum spot temperature for an assumed uniform distribution of e is larger than 0.160 keV (the limit of our model), while the maximum spot temperature for Cen X-4 would be 0.155 keV, both at the spin frequency of 500 Hz. A hot spot temperature larger than 0.160 keV would give a spectroscopically inferred radius less than 50% of the true radius, which essentially means the bias is not usefully bounded.

4.1. Limits of Our Analysis

Our analysis necessarily is limited in scope. Here, we enumerate some complexities that we have not addressed in this work. The temperature distribution of the hot spots may be more complex than we have assumed; especially for large spots, this might cause significant changes (see, e.g., Bauböck et al. 2015b). We have sampled only a few values of the spin period, mass, and radius. We have assumed hydrogen atmospheres; helium atmospheres, while generally similar in spectra and angular dependences, have some subtle differences (see Zavlin et al. 1996, Figures 5 and 9). These issues are unlikely to significantly alter our results.

A larger issue is that we assume that the NS has only one spot. A second spot would reduce the average pulsed fraction, though it would probably not reduce the lower limit on the pulsed fraction substantially (see Section 3). The second spot would generally increase the visible amount of the star at a higher temperature, so it would increase the bias in the radius. Some NSs have strong evidence for poles that are not offset by 180°(e.g., Bogdanov 2013), and/or with different sizes and temperatures (Gotthelf et al. 2010), adding additional possible complexity.

Another major issue is that the distribution of e may not be uniform in either $\cos e$ or in e; if hot spots are more concentrated towards the poles than we assume (as suggested by Lamb et al. 2009), then the pulsed fractions will tend to be lower than we assume.

A final issue, relating to the applicability of our results to other systems, is that our simulations were designed with surface temperature and extinction (N_H) designed to match specific qLMXBs in 47 Tuc. Increased N_H would tend to obscure the softer emission from the full surface more than the hot spot, thus increasing the expected pulsed fraction and the expected bias in spectral fitting.

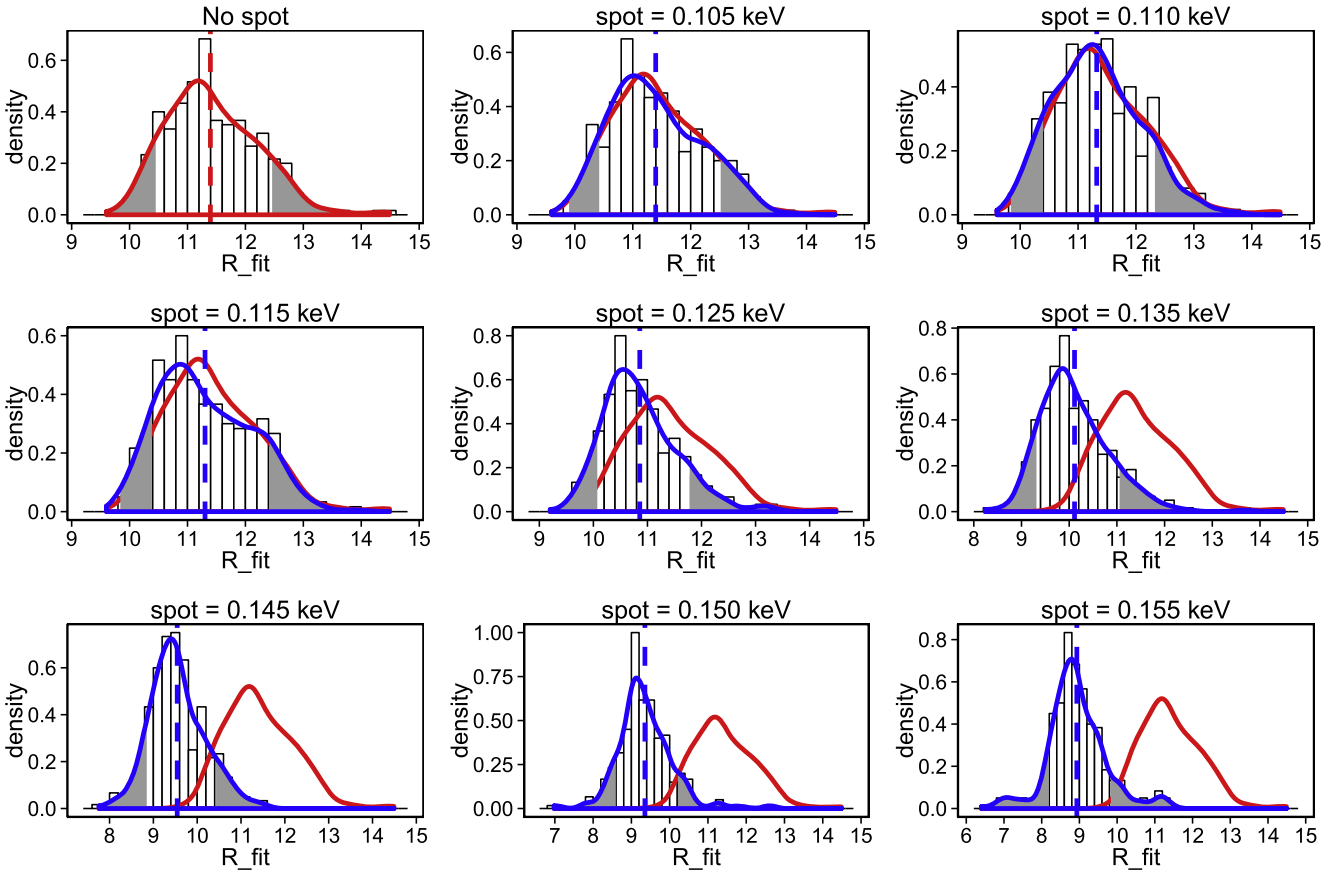

Figure 10. Distribution of ($R_{\rm fit}$) from fitting 300 spectral simulations for different choices of the temperature differential, assuming a 1.4 $M_{\odot}$ NS, with the angles e and i chosen from distributions uniform in $\cos i$ and $\cos e$. The red curve is the probability density curve for the simulations without a hot spot (essentially the systematic errors inherent in the method), while the blue curve indicates the probability density of the inferred $R_{\rm fit}$ at each hot spot temperature. The dashed line is the mean of ($R_{\rm fit}$). The shaded gray areas exclude the upper and lower 10% of each probability density curve. The theoretical model is for a 11.5 km NS spinning at 500 Hz. These histograms show the bias in radii measurements.

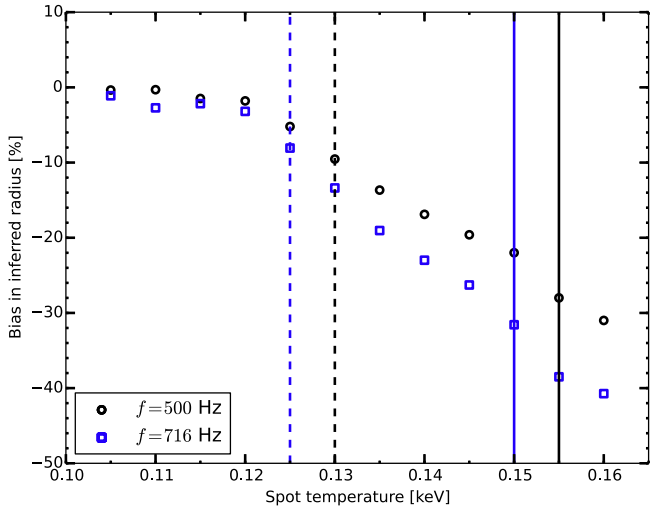

Figure 11. Bias in the spectroscopically inferred $R_{\rm max}$ (90% confidence) as a function of the spot temperature relative to an NS at surface temperature of 0.100 keV. The black color is associated spinning frequency of 500 Hz and the blue color is associated the 716 Hz. The solid and dashed lines are the maximum allowable spot temperatures that would not give rise to detectable pulsations based on the pulsed fraction limits for X7 and Cen-X4, respectively.

5. CONCLUSION

We studied the effects of hot spots on the X-ray light curves, spectra, and spectroscopically inferred masses and radii for NSs with hydrogen atmospheres. Hydrogen atmospheres, due to limb darkening, display higher pulsed fractions than blackbody emission, and so this analysis is necessary in order to constrain the systematic effects of radius measurements on quiescent NSs. We find that the existence of an unmodeled hot spot tends to shift the peak to higher energies, which affects the spectroscopically inferred equatorial radii of NSs.

We first computed the 90% upper limits on the pulsed fractions from 800 ks *Chandra* HRC-S observation for the two sources X5 and X7 in the globular cluster 47 Tuc to be 14% and 13%, respectively, searching spin frequencies <500 Hz. For higher spin frequencies (up to 716 Hz) the limits are 16% and 15%, respectively. We simulated pulsed profiles for ranges of inclination and hot spot emission angles i and e, obtaining the central 90% range of pulsed fraction obtained for different choices of temperature differentials (between the hot spot and the rest of the NS) and NS spin frequencies. This allows us to constrain the maximum temperature differential for any hot spots on X5 and X7. In the case of X7, if we assume it is a 1.4 $M_{\odot}$ NS spinning at 500 Hz, our results indicate that the

maximum allowable temperature differential is 0.055 keV, where >90% of our simulations are above the 90% upper limit of pulsed fraction. The NS in Cen-X4 has a significantly lower upper limit on the pulsed fraction of 6.4%, which puts a tighter constraint on the maximum allowable temperature differential of 0.025 keV. Since the upper limit of source 26 in M28 is high (37%), it does not provide strong constraints.

Finally, we study the effects on the inferred radius of hot spots for these temperature differential limits. The spectroscopically inferred radii of stars with spots tend to be at smaller values than the "true" radius. The 90% confidence range of the inferred radii are generally still consistent with the true value of our fiducial star (11.5 km) for small temperature differentials (0.03 keV).

For the hottest possible hot spots that would not give rise to detectable pulsations in X7, we find that a bias in the best-fit inferred radius of up to 28% smaller than the true radius may be induced by hot spots below our upper limit. For Cen X-4 (where the pulsed fraction constraint is much tighter, <6.4%), downward radius biases are constrained to <10%. If the hot spot emission angle e is distributed uniformly in e (rather than in $\cos e$, as appropriate if the hot spot may be anywhere on the NS surface), then the constraints are significantly looser, and effectively unbounded for the X7 case. Our analysis constrains a key systematic uncertainty in the most promising radius measurement method. We do not know whether quiescent NSs in X-ray binaries without radio pulsar activity have hot spots. However, the possibility strongly motivates further pulsation searches in quiescent NSs in X-ray binaries, particularly those that are targets for spectroscopic radius determination.

The authors are grateful to M. C. Miller and S. Guillot for discussions and comments on the draft, and to S. Ransom for discussions and for providing the PRESTO pulsation search code. C.O.H. has been supported by an NSERC Discovery Grant, an Ingenuity New Faculty Award, and an Alexander von Humboldt Fellowship, and thanks the Max Planck Institute for Radio Astronomy in Bonn for their hospitality. S.M.M. has been supported by an NSERC Discovery Grant. The scientific results reported in this article are based in part on data obtained from the Chandra Data Archive. Support for this work was provided in part by the National Aeronautics and Space Administration through Chandra Award Number AR2-13002X awarded through Columbia University and issued by the Chandra X-ray Observatory Center, which is operated by the Smithsonian Astrophysical Observatory for and on behalf of the National Aeronautics Space Administration under contract NAS8-03060.

REFERENCES

Alcock, C., & Illarionov, A. 1980, ApJ, 235, 534
Antoniadis, J., Freire, P. C. C., Wex, N., et al. 2013, Sci, 340, 448
Bahramian, A., Heinke, C. O., Sivakoff, G. R., et al. 2014, ApJ, 780, 127
Bauböck, M., Özel, F., Psaltis, D., & Morsink, S. M. 2015a, ApJ, 799, 22
Bauböck, M., Psaltis, D., & Özel, F. 2015b, ApJ, 811, 144
Becker, W., Swartz, D. A., Pavlov, G. G., et al. 2003, ApJ, 594, 798
Bhattacharya, D., & van den Heuvel, E. P. J. 1991, PhR, 203, 1
Bhattacharyya, S. 2010, AdSpR, 45, 949
Bogdanov, S. 2013, ApJ, 762, 96
Bogdanov, S., Archibald, A. M., Hessels, J. W. T., et al. 2011, ApJ, 742, 97
Bogdanov, S., Heinke, C. O., Özel, F., & Güver, T. 2016, arXiv:1603.01630
Bogdanov, S., Rybicki, G. B., & Grindlay, J. E. 2007, ApJ, 670, 668
Brown, E. F., Bildsten, L., & Rutledge, R. E. 1998, ApJL, 504, L95
Cackett, E. M., Brown, E. F., Miller, J. M., & Wijnands, R. 2010, ApJ, 720, 1325
Cadeau, C., Morsink, S. M., Leahy, D., & Campbell, S. S. 2007, ApJ, 654, 458
Cameron, P. B., Rutledge, R. E., Camilo, F., et al. 2007, ApJ, 660, 587
Campana, S., Stella, L., Mereghetti, S., et al. 1998, ApJL, 499, L65
Catuneanu, A., Heinke, C. O., Sivakoff, G. R., Ho, W. C. G., & Servillat, M. 2013, ApJ, 764, 145
Chakrabarty, D., Tomsick, J. A., Grefenstette, B. W., et al. 2014, ApJ, 797, 92
Chen, K., & Ruderman, M. 1993, ApJ, 408, 179
Chen, K., Ruderman, M., & Zhu, T. 1998, ApJ, 493, 397
Chevalier, C., Ilovaisky, S. A., van Paradijs, J., Pedersen, H., & van der Klis, M. 1989, A&A, 210, 114
Damen, E., Magnier, E., Lewin, W. H. G., et al. 1990, A&A, 237, 103
D'Angelo, C. R., Fridriksson, J. K., Messenger, C., & Patruno, A. 2015, MNRAS, 449, 2803
Davis, J. E. 2001, ApJ, 562, 575
De Luca, A., Caraveo, P. A., Mereghetti, S., Negroni, M., & Bignami, G. F. 2005, ApJ, 623, 1051
Demorest, P. B., Pennucci, T., Ransom, S. M., Roberts, M. S. E., & Hessels, J. W. T. 2010, Natur, 467, 1081
Deufel, B., Dullemond, C. P., & Spruit, H. C. 2001, A&A, 377, 955
Edmonds, P. D., Heinke, C. O., Grindlay, J. E., & Gilliland, R. L. 2002, ApJL, 564, L17
Freire, P. C. C., Bassa, C. G., Wex, N., et al. 2011, MNRAS, 412, 2763
Galloway, D. K., & Lampe, N. 2012, ApJ, 747, 75
Geppert, U., Küker, M., & Page, D. 2004, A&A, 426, 267
Gierliński, M., Done, C., & Barret, D. 2002, MNRAS, 331, 141
Gotthelf, E. V., Perna, R., & Halpern, J. P. 2010, ApJ, 724, 1316
Gratton, R. G., Bragaglia, A., Carretta, E., et al. 2003, A&A, 408, 529
Greenstein, J. L., Dolez, N., & Vauclair, G. 1983, A&A, 127, 25
Grindlay, J. E., Heinke, C., Edmonds, P. D., & Murray, S. S. 2001, Sci, 292, 2290
Guillot, S., Rutledge, R. E., Brown, E. F., Pavlov, G. G., & Zavlin, V. E. 2011, ApJ, 738, 129
Guillot, S., Servillat, M., Webb, N. A., & Rutledge, R. E. 2013, ApJ, 772, 7
Güver, T., Özel, F., Cabrera-Lavers, A., & Wroblewski, P. 2010a, ApJ, 712, 964
Güver, T., Wroblewski, P., Camarota, L., & Özel, F. 2010b, ApJ, 719, 1807
Haakonsen, C. B., Turner, M. L., Tacik, N. A., & Rutledge, R. E. 2012, ApJ, 749, 52
Haensel, P., Bejger, M., Fortin, M., & Zdunik, L. 2016, EPJA, 52, 59
Haggard, D., Cool, A. M., Anderson, J., et al. 2004, ApJ, 613, 512
Hameury, J. M., Heyvaerts, J., & Bonazzola, S. 1983, A&A, 121, 259
Hansen, B. M. S., Kalirai, J. S., Anderson, J., et al. 2013, Natur, 500, 51
Harding, A. K., Strickman, M. S., Gwinn, C., et al. 2002, ApJ, 576, 376
Hasinger, G., Johnston, H. M., & Verbunt, F. 1994, A&A, 288, 466
Hebeler, K., Lattimer, J. M., Pethick, C. J., & Schwenk, A. 2013, ApJ, 773, 11
Heinke, C. O., Cohn, H. N., Lugger, P. M., et al. 2014, MNRAS, 444, 443
Heinke, C. O., Grindlay, J. E., Lloyd, D. A., & Edmonds, P. D. 2003, ApJ, 588, 452
Heinke, C. O., Rybicki, G. B., Narayan, R., & Grindlay, J. E. 2006, ApJ, 644, 1090
Hertz, P., & Grindlay, J. E. 1983, ApJ, 275, 105
Hessels, J. W. T., Ransom, S. M., Stairs, I. H., et al. 2006, Sci, 311, 1901
Johnson, T. J., Venter, C., Harding, A. K., et al. 2014, ApJS, 213, 6
Lamb, F. K., Boutloukos, S., Van Wassenhove, S., et al. 2009, ApJ, 706, 417
Lattimer, J. M., & Prakash, M. 2001, ApJ, 550, 426
Lattimer, J. M., & Prakash, M. 2007, PhR, 442, 109
Lattimer, J. M., & Prakash, M. 2016, PhR, 621, 127
Lattimer, J. M., & Steiner, A. W. 2014, ApJ, 784, 123
Leahy, D. A., Darbro, W., Elsner, R. F., et al. 1983, ApJ, 266, 160
Lewin, W. H. G., van Paradijs, J., & Taam, R. E. 1993, SSRv, 62, 223
Lloyd, D. A. 2003, arXiv:astro-ph/0303561
Lyne, A., & Graham-Smith, F. 2006, Pulsar Astronomy (Cambridge: Cambridge Univ. Press)
Manchester, R. N., & Han, J. L. 2004, ApJ, 609, 354
Manzali, A., De Luca, A., & Caraveo, P. A. 2007, ApJ, 669, 570
McClintock, J. E., Narayan, R., & Rybicki, G. B. 2004, ApJ, 615, 402
Messenger, C. 2011, PhRvD, 84, 083003
Middleditch, J. 1976, PhD thesis, California Univ.
Miller, M. C., & Lamb, F. K. 1998, ApJL, 499, L37
Miller, M. C., & Miller, J. M. 2015, PhR, 548, 1
Morsink, S. M., Leahy, D. A., Cadeau, C., & Braga, J. 2007, ApJ, 663, 1244
Nättilä, J., Steiner, A. W., Kajava, J. J. E., Suleimanov, V. F., & Poutanen, J. 2015, arXiv:1509.06561
Özel, F. 2006, Natur, 441, 1115

Özel, F. 2013, RPPh, 76, 016901
Özel, F., Güver, T., & Psaltis, D. 2009, ApJ, 693, 1775
Özel, F., Psaltis, D., Güver, T., et al. 2016, ApJ, 820, 28
Papitto, A., Ferrigno, C., Bozzo, E., et al. 2013, Natur, 501, 517
Pavlov, G. G., Shibanov, Y. A., Ventura, J., & Zavlin, V. E. 1994, A&A, 289, 837
Pechenick, K. R., Ftaclas, C., & Cohen, J. M. 1983, ApJ, 274, 846
Pons, J. A., Walter, F. M., Lattimer, J. M., et al. 2002, ApJ, 564, 981
Potekhin, A. Y., & Yakovlev, D. G. 2001, A&A, 374, 213
Poutanen, J., & Gierliński, M. 2003, MNRAS, 343, 1301
Poutanen, J., Nättilä, J., Kajava, J. J. E., et al. 2014, MNRAS, 442, 3777
Predehl, P., Hasinger, G., & Verbunt, F. 1991, A&A, 246, L21
Psaltis, D., Özel, F., & Chakrabarty, D. 2014, ApJ, 787, 136
Psaltis, D., Özel, F., & DeDeo, S. 2000, ApJ, 544, 390
Rajagopal, M., & Romani, R. W. 1996, ApJ, 461, 327
Ransom, S. M. 2002, in ASP Conf. Ser. 271, Neutron Stars in Supernova Remnants, ed. P. O. Slane & B. M. Gaensler (San Francisco, CA: ASP), 361
Ransom, S. M., Cordes, J. M., & Eikenberry, S. S. 2003, ApJ, 589, 911
Ransom, S. M., Greenhill, L. J., Herrnstein, J. R., et al. 2001, ApJL, 546, L25
Ransom, S. M., Stairs, I. H., Archibald, A. M., et al. 2014, Natur, 505, 520
Romani, R. W. 1987, ApJ, 313, 718
Rutledge, R. E., Bildsten, L., Brown, E. F., Pavlov, G. G., & Zavlin, V. E. 2002, ApJ, 578, 405
Rutledge, R. E., Fox, D. W., Kulkarni, S. R., et al. 2004, ApJ, 613, 522
Servillat, M., Heinke, C. O., Ho, W. C. G., et al. 2012, MNRAS, 423, 1556
Steiner, A. W., Lattimer, J. M., & Brown, E. F. 2010, ApJ, 722, 33
Steiner, A. W., Lattimer, J. M., & Brown, E. F. 2016, EPJA, 52, 18
Suleimanov, V., Poutanen, J., & Werner, K. 2011, A&A, 527, A139
Sztajno, M., Fujimoto, M. Y., van Paradijs, J., et al. 1987, MNRAS, 226, 39
van Paradijs, J. 1979, ApJ, 234, 609
Vaughan, B. A., van der Klis, M., Wood, K. S., et al. 1994, ApJ, 435, 362
Verbunt, F., & Hasinger, G. 1998, A&A, 336, 895
Webb, N. A., & Barret, D. 2007, ApJ, 671, 727
Wilms, J., Allen, A., & McCray, R. 2000, ApJ, 542, 914
Woodley, K. A., Goldsbury, R., Kalirai, J. S., et al. 2012, AJ, 143, 50
Worpel, H., Galloway, D. K., & Price, D. J. 2013, ApJ, 772, 94
Zamfir, M., Cumming, A., & Galloway, D. K. 2012, ApJ, 749, 69
Zavlin, V. E., & Pavlov, G. G. 2002, in MPE Report 278, Proc. of the 270 WE-Heraeus Seminar on Neutron Stars, Pulsars, and Supernova Remnants, ed. W. Becker, H. Lesch, & J. Trümper (Garching: Max-Plank-Institut für extraterrestrische Physik), 263
Zavlin, V. E., Pavlov, G. G., Sanwal, D., & Trümper, J. 2000, ApJL, 540, L25
Zavlin, V. E., Pavlov, G. G., & Shibanov, Y. A. 1996, A&A, 315, 141